

ANALYTICAL AND NUMERICAL STUDY OF PHOTOCURRENT TRANSIENTS IN ORGANIC POLYMER SOLAR CELLS

CARLO DE FALCO, RICCARDO SACCO, AND MAURIZIO VERRI

ABSTRACT. This article is an attempt to provide a self consistent picture, including existence analysis and numerical solution algorithms, of the mathematical problems arising from modeling photocurrent transients in Organic-polymer Solar Cells (OSCs). The mathematical model for OSCs consists of a system of nonlinear diffusion-reaction partial differential equations (PDEs) with electrostatic convection, coupled to a kinetic ordinary differential equation (ODE). We propose a suitable reformulation of the model that allows us to prove the existence of a solution in both stationary and transient conditions and to better highlight the role of exciton dynamics in determining the device turn-on time. For the numerical treatment of the problem, we carry out a temporal semi-discretization using an implicit adaptive method, and the resulting sequence of differential subproblems is linearized using the Newton-Raphson method with inexact evaluation of the Jacobian. Then, we use exponentially fitted finite elements for the spatial discretization, and we carry out a thorough validation of the computational model by extensively investigating the impact of the model parameters on photocurrent transient times.

1. INTRODUCTION AND MOTIVATION

A continuously growing attention has been paid over the last years by the international community and government authorities to monitoring the effect of the increase of global concentrations of carbon dioxide, methane and nitrous oxide on the quality of our everyday life. The results of the investigation carried out by the Intergovernmental Panel on Climate Change [1] have brought the European Union (EU) to the decision that carbon dioxide emissions should decrease by 20 percent, and that 20 percent of the energy produced in EU should originate from renewable energy sources, such as wind, water, biomass, and solar, not later than 2020 [2]. In this perspective, research and design of third generation (3G) photovoltaic devices [3] for solar energy conversion into electrical and thermal energy turns out to be a central topic in the wider area of renewable energy sources. Roughly speaking, 3G photovoltaic devices can be divided into two main classes: electrochemical cells [4, 5, 6] and organic-polymer cells [7, 8, 9] which are the topic of the present article. Most of investigation activity in solar cell design is devoted to the experimental study of innovative materials for efficient and flexible technologies, and is not presently accompanied by a systematic use of computational models to predict and optimize their performance. This article is an attempt to fill this gap by introducing the numerical engineering community to the mathematical problems that arise in the context of modeling and simulation of OSCs. With this aim, we try to provide a reasonably self-contained picture of the topic, including a discussion of the peculiarities of the model, an analysis of the existence of a solution, and the description of a robust computational algorithm to compute such solution. In particular, we focus on a special class of OSCs, namely that of Bulk Hetero-Junction (BHJ) devices, that

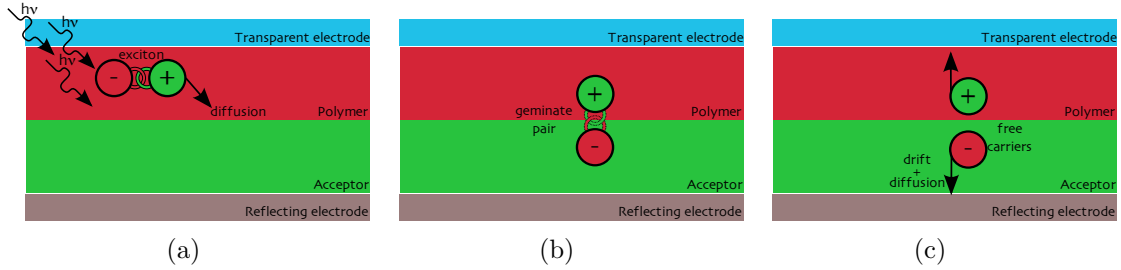


FIGURE 1. Working principle of OSCs.

currently represent the most promising technology in terms of energy conversion efficiency [9, 8]. Charge transport in BHJs is described by a set of nonlinear PDEs of diffusion-reaction type with electrostatic convection coupled with a kinetic ODE for the temporal evolution of exciton concentration in the cell [10, 11, 12, 13]. Sect. 2 is devoted to the description of the structure and working principles of BHJs while in Sect. 3 the mathematical model is introduced and the connection between its features and the physical phenomena involved in photocurrent generation is drawn. Some effort is also put into highlighting the main differences between the problem at hand and the case of more standard crystalline inorganic semiconductor devices. In Sect. 4, under suitable assumptions on the model coefficients, *i*) we prove the existence of a solution of the problem in stationary conditions; and *ii*) we derive a simplified model in transient conditions, that is amenable for a qualitative analysis of the time response of the device, and for which we again prove existence of a solution. For the numerical treatment of the problem, which is the topic of Sect. 5, we carry out a temporal semi-discretization using an implicit adaptive method, and the resulting sequence of differential subproblems is linearized using the Newton-Raphson method with inexact evaluation of the Jacobian. Then, we use exponentially fitted finite elements for the spatial discretization, to ensure a stable approximation of the internal and boundary layers arising in the distribution profile of the photogenerated carriers. The numerical experiments of Sect. 6 are meant, on the one hand, to illustrate the complex interplay among different physical phenomena determining the photocurrent turn-on transient time of a realistic BHJ cell in different regimes and, on the other hand, to characterize the range of applicability of the reduced model introduced in Sect. 4. In Sect. 7 we address some concluding remarks and indicate possible future research directions.

2. BULK HETEROJUNCTION ORGANIC SOLAR CELLS

Before presenting the mathematical model which is the main focus of this paper, a schematic description of working principle of OSCs, and in particular of those with a BHJ structure, is in order. For more details on the subject the interested reader is referred to [9, 8]. The simplest possible structure for an organic-polymer based solar cell is depicted in Fig. 1: two thin films composed of a conjugated organic polymer and of a material with high electron affinity, usually referred to as a *acceptor* are sandwiched between one transparent (*e.g.* indium-tin-oxide or fluorinated tin oxide) and one reflecting metal contact (usually aluminum or silver). When illuminated, electrons in the Highest Occupied Molecular Orbital (HOMO) in the polymer are promoted to the Lowest Unoccupied Molecular Orbital (LUMO) thus forming an

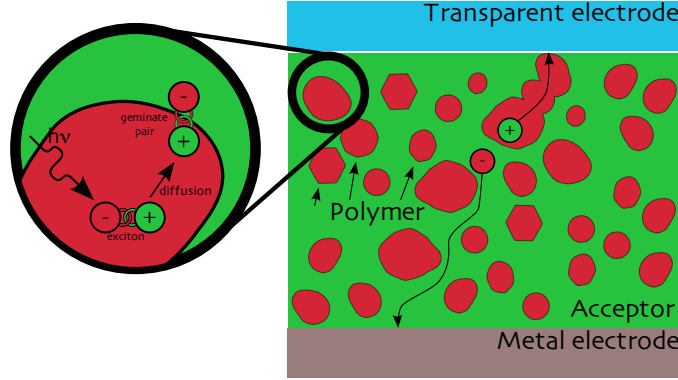


FIGURE 2. Bulk Heterojunction OSCs.

electron-hole pair. Such pair, which we refer to as an *exciton* (Fig. 1(a)), in contrast to what is usually the case in standard inorganic semiconductors, is electrically neutral and has very strong binding energy (of the order of 1eV) with a radius in the sub-nanometer range. The *diffusion length* λ_X of a moving exciton in commonly used polymeric materials is of the order of a few nanometers. An exciton has a non-negligible chance of eventually reaching the polymer/acceptor interface only if it was photo-generated within a distance $\leq \lambda_X$. In case this occurs, the built-in chemical potential drop produced by the difference in electron affinity between the two materials is strong enough to *stretch* the exciton driving the electron and hole to a distance of the order of 1nm thus reducing the strength of their Coulomb attraction. This less tightly bound electron-hole pair is referred to in the literature as a *geminate pair* (Fig. 1(b)) and the energy of the bond is low enough that it can be overcome by the electric field induced by a small voltage difference applied at the contacts. The newly separated electron and hole migrate, driven by electric field drift and diffusion forces, to the anode and cathode, respectively, where they are *harvested* thus producing a net current (Fig. 1(c)). The currently investigated most promising device technology to maximize the efficiency of the photogeneration process is the BHJ cell depicted in Fig. 2 which is produced by spin-casting both the polymer (usually rr-P3HT or MDMO-PPV) and the acceptor (usually some derivative of fullerene or inorganic nanoparticles, *e.g.* titanium-dioxide) from a common solution. This process results in a highly folded structure that has the advantage that all photo-generated excitons eventually reach an interface, at the price of reducing the *effective* carrier mobility because of the convoluted path that carriers need to travel to reach the contacts. Also, from a perspective that is more relevant to the topic of this paper, the highly disordered structure of BHJs makes it difficult to characterize model parameters, as an averaging over the highly disordered nanostructure of the device would be required. Therefore the typical approach is to estimate the parameter values experimentally and resort to numerical simulations to properly interpret the measurement results.

3. THE MATHEMATICAL MODEL

In this section we illustrate the mathematical model of the photogeneration mechanisms that drive charge transport in BHJ solar cells (see [10, 9, 11, 12, 13]). The

polymer/acceptor blend is represented by a homogeneous material filling a bounded domain $\Omega \subset \mathbb{R}^d$, $d \geq 1$, with a Lipschitz boundary $\Gamma \equiv \partial\Omega$ divided into two disjoint subregions, Γ_D and Γ_N , representing the interface between metal and polymer blend and interior artificial boundaries, respectively. We assume that $\text{meas}(\Gamma_D) > 0$ and $\Gamma_D \cap \Gamma_N = \emptyset$, and denote by $\boldsymbol{\nu}$ the outward unit normal vector along Γ .

3.1. Governing Equations. Charge transport in the device is governed by the set of continuity equations

$$(1a) \quad \begin{cases} \frac{\partial n}{\partial t} - \text{div} \mathbf{J}_n = G_n - R_n n \\ \frac{\partial p}{\partial t} - \text{div} \mathbf{J}_p = G_p - R_p p \end{cases} \quad \text{in } \Omega_T,$$

where $\Omega_T \equiv \Omega \times (0, T)$, $T > 0$, n and p denote the *electron and hole density*, respectively. Using from now on the symbol η to indicate either of n or p , \mathbf{J}_η are the corresponding *flux densities*, G_η , are the carrier *generation rates*, and $R_\eta \eta$ are the *recombination rates*. As electrons are negatively charged while hole charge is positive, the *total current density* \mathbf{J} can be expressed as $\mathbf{J} = q(\mathbf{J}_p - \mathbf{J}_n)$ where $q > 0$ is the magnitude of the electron charge. The charge carrier flux densities are, in turn, each composed of an *electrostatic drift* term and a *diffusion* term

$$(1b) \quad \begin{cases} \mathbf{J}_n = D_n \nabla n - \mu_n n \nabla \varphi \\ \mathbf{J}_p = D_p \nabla p + \mu_p p \nabla \varphi \end{cases} \quad \text{in } \Omega_T,$$

D_η being the charge carrier *diffusion coefficients* and μ_η the *carrier mobilities*. The *electrostatic potential* φ satisfies the Poisson equation

$$(1c) \quad -\text{div}(\varepsilon \nabla \varphi) = q(p - n) \quad \text{in } \Omega_T,$$

where ε is the (averaged) dielectric permittivity of the blend. Notice that, as there are usually no dopants in organic cells, the net charge density on the right-hand-side in (1c) is given by the carrier densities only. We denote by X the *volume density of geminate pairs* and we express its rate of change as

$$(1d) \quad \frac{\partial X}{\partial t} = g - r \quad \text{in } \Omega_T.$$

The geminate-pair generation rate g in (1d) can be split into two contributions as

$$(2) \quad g = \underbrace{G(\mathbf{x}, t)}_{(a)} + \underbrace{\gamma p n}_{(b)},$$

(a) accounting for the rate at which excitons reach the material interfaces and are partially separated and (b) accounting for the rate at which free electrons and holes are attracted to each other and recombine. Process (b) is referred to as *bimolecular recombination* and the coefficient γ is described according to the Langevin theory [7]. The rate of process (a) is equal to the rate $G(\mathbf{x}, t)$ at which photons are absorbed, which we assume in what follows to be a known function of position and time. As in BHJ all excitons are eventually transformed in geminate pairs it is legitimate, with a slight abuse of notation, to use in the following the two terms as synonyms. As for the term r in (1d) it can also be split into two contributions as

$$(3) \quad r = \underbrace{k_{diss} X}_{(c)} + \underbrace{k_{rec} X}_{(d)},$$

(c) accounting for the rate at which geminate pairs that are not split recombine and (d) accounting for the rate at which free electrons and holes are produced by separation of a bound pair. We assume the coefficient k_{rec} to be a given constant while k_{diss} depends on the magnitude of the electric field $\mathbf{E} = -\nabla\varphi$ as described in [7]. As we assume free carriers to be generated only by dissociation of a geminate pair and to be annihilated only by recombination into a geminate pair, the generation rates satisfy $G_n = G_p = k_{diss}X$ while for the recombination rates $R_n n = R_p p = \gamma p n$ holds.

We wish at this point to stress some peculiarities of the model we have introduced compared to the standard case of crystalline inorganic semiconductors. The main difference is represented by the strong influence that the exciton reaction kinetics described by equation (1d) has on device performance. Indeed, such a kinetics affects both the energy conversion efficiency in the steady state operation and the turn-on transient time. This latter, in particular, is relevant for the characterization of material properties that can not be determined by first-principles because of the highly convoluted device nanostructure. Furthermore, although equations (1a)-(1b) are analogous to those describing charge transport in ordered inorganic semiconductors, the physical driving mechanisms at the microscopic level are quite different. In particular, while in monocrystalline semiconductors charge carriers are essentially free to move within *delocalized* orbitals, in the materials we study here transport happens via *hopping* of charges between *localized* orbitals. This microscopic difference is reflected in the macroscopic models for the diffusion and mobility coefficients for organic semiconductor materials which (i) introduce very different dependencies on temperature and electric field magnitude [14, 15], and (ii) introduce a dependency of the mobility on the carrier densities [13].

3.2. Boundary and Initial Conditions. A delicate and important issue is that of devising a set of boundary conditions to accurately describe the complex phenomena of charge injection and recombination occurring at the interface Γ_D separating the metal contacts from the semiconductor bulk. Precisely, according to [16, 10], such conditions are expressed in the following Robin-type form

$$(4a) \quad \kappa_n \mathbf{J}_n \cdot \boldsymbol{\nu} = \beta_n - \alpha_n n \quad \text{on } \Gamma_D \times (0, T)$$

$$(4b) \quad \kappa_p \mathbf{J}_p \cdot \boldsymbol{\nu} = \beta_p - \alpha_p p \quad \text{on } \Gamma_D \times (0, T),$$

where κ_η are non negative parameters while β_η are the rates at which charges are injected into the device and $\alpha_\eta \eta$ are the rates at which electrons and holes recombine with their image charges at the contacts, respectively. Reliable models for the above parameters are still subject of extensive investigation as the basic description proposed in the milestone reference [16] needs to be modified via empirical fitting to avoid the occurrence of unphysical behavior in the computed solution [12, 17]. As for the electric potential, the Dirichlet condition

$$(4c) \quad \varphi = \Psi_D \quad \text{on } \Gamma_D \times (0, T)$$

is enforced, where the datum Ψ_D accounts for both the externally applied voltage and the work-function difference between the contact materials. On Γ_N , which represents the interior artificial boundary, homogeneous Neumann conditions for the flux densities and the electric field are imposed. Finally, positive initial conditions

$n(\mathbf{x}, 0) = n_0(\mathbf{x})$, $p(\mathbf{x}, 0) = p_0(\mathbf{x})$, and $X(\mathbf{x}, 0) = X_0(\mathbf{x})$ are needed to complete the mathematical model.

4. SYSTEM ANALYSIS OF THE MODEL

In this section, we deal with the analysis of the existence of a solution of system (1a)-(1d) in both stationary and transient regimes, under the following assumptions:

- (H1): γ , k_{diss} , k_{rec} and G are all positive constant quantities in Ω_T ;
- (H2): $D_\eta = V_{th}\mu_\eta$, V_{th} being the *thermal voltage* and $\mu_\eta \geq \mu_{\eta_0} > 0$ a.e. in Ω_T ;
- (H3): $v_n, v_p \leq v^{max} < +\infty$ where $v_\eta := \mu_\eta |\mathbf{E}|$;
- (H4): $\kappa_\eta = 0$ and α_η, β_η are functions of position only in (4a)-(4b).

Although the purpose of the set of hypotheses (H1)-(H4) is mainly to reduce the mathematical complexity of the problem, we wish here to comment about their physical plausibility. Assumption (H1) allows us to express in an easy manner the dependent variable X as a function of n , p and of the input data G and X_0 , in such a way that the resulting equivalent system (in the reduced set of unknowns φ , n and p) can be written in the form of a two-carrier drift-diffusion (DD) model. As the coefficients involved in (H1) depend, in general, only on the magnitude of the electric field, such an assumption is reasonable if the field itself varies weakly within the simulation domain, which is often the case in realistic photovoltaic devices as is confirmed by the numerical experiments of Sect. 6. Assumption (H2) is the classical Einstein relation valid in inorganic semiconductors and corresponds to neglecting the (higher order) effect of energetic disorder [13]. The saturation of convective velocities expressed by assumption (H3) is reasonable in a structure that is highly folded as that of BHJs and is indeed commonly employed in commercial packages for organic semiconductor simulation [18]. Assumption (H4) corresponds to an infinite carrier recombination rate at the contacts.

4.1. Stationary Regime. Setting $\partial X/\partial t = 0$ in (1d), we can eliminate the dependent variable X in favor of n , p and of the input function G , to obtain

$$(5) \quad X(\mathbf{x}) = \tau G + \gamma \tau p(\mathbf{x}) n(\mathbf{x})$$

where

$$(6) \quad \tau := \frac{1}{k_{diss} + k_{rec}}$$

is the time of response of the generation/recombination terms to light stimuli. Using (5)-(6) and (H4), the stationary OSC model reads:

$$(7) \quad \begin{cases} -\operatorname{div}(\varepsilon \nabla \varphi) &= q(p - n) \\ -\operatorname{div} \mathbf{J}_n &= \tau (k_{diss} G - \gamma k_{rec} p n) \\ -\operatorname{div} \mathbf{J}_p &= \tau (k_{diss} G - \gamma k_{rec} p n), \end{cases} \quad \text{in } \Omega$$

supplied with the boundary conditions

$$(8) \quad \begin{cases} \varphi = \Psi_D, \quad n = n_D := \frac{\beta_n}{\alpha_n}, \quad p = p_D := \frac{\beta_p}{\alpha_p} & \text{on } \Gamma_D \\ \mathbf{J}_n \cdot \boldsymbol{\nu} = \mathbf{J}_p \cdot \boldsymbol{\nu} = \nabla \varphi \cdot \boldsymbol{\nu} = 0 & \text{on } \Gamma_N. \end{cases}$$

Theorem 1 (Existence of a solution in stationary regime). *Let assumptions (H1)–(H4) be satisfied and $(\Psi_D, n_D, p_D) \in (L^\infty(\Gamma_D))^3$. Then, problem (7)–(8) admits a weak solution $(\varphi^*, u^*, v^*) \in (H^1(\Omega) \cap L^\infty(\Omega))^3$ and there exist positive constants $\underline{\mathcal{M}}, \underline{\mathcal{K}}, \bar{\mathcal{K}}$ such that*

$$(9) \quad \underline{\mathcal{M}} \leq n^*, p^* \leq \bar{\mathcal{M}}, \quad \underline{\mathcal{K}} \leq \varphi^* \leq \bar{\mathcal{K}} \quad \text{a.e. in } \Omega.$$

The proof of Theorem 1 follows closely the guidelines of [19], Sect.3.3 and is sketched below. Using (H2) we can write the two flux densities as

$$(10) \quad \begin{cases} \mathbf{J}_n &= \mu_n V_{th} n_r e^{\varphi/V_{th}} \nabla u, \\ \mathbf{J}_p &= \mu_p V_{th} n_r e^{-\varphi/V_{th}} \nabla v, \end{cases}$$

where the new (dimensionless) dependent variables u and v are related to the carrier densities n and p by the Maxwell–Boltzmann statistics

$$(11) \quad n = n_r u e^{\varphi/V_{th}}, \quad p = n_r v e^{-\varphi/V_{th}},$$

$n_r > 0$ being a reference concentration. System (7)–(8) then becomes:

$$(12) \quad \begin{cases} -\operatorname{div}(\varepsilon \nabla \varphi) &= q n_r (u e^{\varphi/V_{th}} - v e^{-\varphi/V_{th}}) \\ -\operatorname{div}(\mu_n V_{th} e^{\varphi/V_{th}} \nabla u) &= \frac{\tau k_{diss} G}{n_r} (1 - uv) \\ -\operatorname{div}(\mu_p V_{th} e^{-\varphi/V_{th}} \nabla v) &= \frac{\tau k_{diss} G}{n_r} (1 - uv) \end{cases} \quad \text{in } \Omega$$

and

$$(13) \quad \begin{cases} \varphi = \Psi_D, \quad u = u_D := \frac{n_D}{n_r} e^{-\Psi_D/V_{th}}, \quad v = v_D := \frac{p_D}{n_r} e^{\Psi_D/V_{th}} & \text{on } \Gamma_D \\ \mathbf{J}_n \cdot \boldsymbol{\nu} = \mathbf{J}_p \cdot \boldsymbol{\nu} = \nabla \varphi \cdot \boldsymbol{\nu} = 0 & \text{on } \Gamma_N. \end{cases}$$

Using the boundedness of the Dirichlet data, the positivity of n_D and p_D and choosing n_r in such a way that $(\gamma k_{rec} n_r^2)/(k_{diss} G) = 1$, we can see that

$$(14) \quad e^{-\Psi^+/V_{th}} \leq u_D, \quad v_D \leq e^{\Psi^+/V_{th}} \quad \text{a.e. on } \Gamma_D,$$

where

$$\Psi^+ := \max \left\{ \max(\sup_{\Gamma_D}(-\varphi_{nD}), \sup_{\Gamma_D}(\varphi_{pD})), -\min(\inf_{\Gamma_D}(-\varphi_{nD}), \inf_{\Gamma_D}(\varphi_{pD})) \right\}$$

and

$$\varphi_{nD} := \Psi_D - V_{th} \ln(n_D/n_r), \quad \varphi_{pD} := \Psi_D + V_{th} \ln(p_D/n_r).$$

Then, by applying Theorem 3.3.16 of [19] to system (12)–(13) and going back to the original variables n and p via the inversion of (11), we conclude that Theorem 1 holds with

$$(15a) \quad \underline{\mathcal{K}} = n_r e^{-\hat{\Psi}^+/V_{th}}, \quad \bar{\mathcal{K}} = n_r e^{\hat{\Psi}^+/V_{th}}$$

$$(15b) \quad \underline{\mathcal{M}} = \min \left(\inf_{\Gamma_D} \Psi_D, -\Psi^+ \right), \quad \bar{\mathcal{M}} = \max \left(\sup_{\Gamma_D} \Psi_D, \Psi^+ \right)$$

where $\hat{\Psi}^+ := \sup_{\Gamma_D} |\Psi_D| + \Psi^+$.

4.2. Transient Regime. Analogously to what we have done in Sect. 4.1 in the stationary case, we can use (1d) to eliminate the dependent variable X in favor of n , p and of the input functions G and X_0 , to obtain

$$(16) \quad X(\mathbf{x}, t) = \xi(\mathbf{x}, t) + \gamma \int_0^t p(\mathbf{x}, s) n(\mathbf{x}, s) e^{-(t-s)/\tau} ds,$$

where $\xi(\mathbf{x}, t) := X_0(\mathbf{x})e^{-t/\tau} + \tau G(1 - e^{-t/\tau})$. The quadratic convolution term in (16) makes the dependence of the current on the electron and hole densities non-local in time with a “memory window” of size proportional to τ . For the subsequent existence analysis it is convenient to manipulate such term so that we can write the continuity equations in the following equivalent form:

$$(17) \quad \begin{cases} \frac{\partial n}{\partial t} - \operatorname{div} \mathbf{J}_n = k_{diss} \xi - \gamma \tau (k_{rec} + k_{diss} e^{-t/\tau}) p n + I \\ \frac{\partial p}{\partial t} - \operatorname{div} \mathbf{J}_p = k_{diss} \xi - \gamma \tau (k_{rec} + k_{diss} e^{-t/\tau}) p n + I, \end{cases}$$

where

$$(18) \quad I := \gamma k_{diss} \int_0^t [p(\mathbf{x}, s) n(\mathbf{x}, s) - p(\mathbf{x}, t) n(\mathbf{x}, t)] e^{-(t-s)/\tau} ds.$$

Although I is no more a convolution integral, it has the interesting property of vanishing both at $t = 0$ and $t = +\infty$, from which we expect, at least formally, that replacing the integral I by a suitable approximation, say \tilde{I} , should not have a significant impact on the model behaviour as long as it preserves the asymptotics of I . Our choice is to use a trapezoidal quadrature rule, yielding

$$(19) \quad I \simeq \tilde{I} = \gamma k_{diss} \frac{t}{2} e^{-t/\tau} [p(\mathbf{x}, 0) n(\mathbf{x}, 0) - p(\mathbf{x}, t) n(\mathbf{x}, t)].$$

It is easy to see that \tilde{I} vanishes both at $t = 0$ and $t = +\infty$; moreover, the approximate formula (19) as the advantage of *lumping* the non-locality of I into a quadratic term that has the same form as the generation/recombination rates already present in the right-hand side of (17). The resulting reduced model reads:

$$(20) \quad \begin{cases} -\operatorname{div}(\varepsilon \nabla \varphi) &= q(p - n) \\ \frac{\partial n}{\partial t} - \operatorname{div} \mathbf{J}_n &= \tilde{G}_n - \tilde{R}_n n \\ \frac{\partial p}{\partial t} - \operatorname{div} \mathbf{J}_p &= \tilde{G}_p - \tilde{R}_p p, \end{cases} \quad \text{in } \Omega_T$$

where the modified generation/recombination mechanisms are defined as

$$(21) \quad \begin{cases} \tilde{G}_n &= \tilde{G}_p = k_{diss} \xi(\mathbf{x}, t) + \gamma k_{diss} \frac{t}{2} e^{-t/\tau} p(\mathbf{x}, 0) n(\mathbf{x}, 0) \\ \tilde{R}_n n &= \tilde{R}_p p = \gamma \left[\tau (k_{rec} + k_{diss} e^{-t/\tau}) + k_{diss} \frac{t}{2} e^{-t/\tau} \right] p(\mathbf{x}, t) n(\mathbf{x}, t). \end{cases}$$

Having derived a new, simplified model, it is natural to ask to which extent the novel formulation is capable to describe correctly the main features of the performance of an OSC. With this aim, we first investigate the quality of the approximation

provided by \tilde{I} ; the quadrature error associated with the use of the trapezoidal rule in (19) is given by the following relation [20]

$$(22) \quad E(t) = -\frac{t^3}{12} e^{-(t-\zeta)/\tau} \left(\lambda''(\zeta) + \frac{2}{\tau} \lambda'(\zeta) + \frac{1}{\tau^2} (\lambda(\zeta) - \lambda(t)) \right)$$

where $\zeta \in (0, t)$ and $\lambda(s) := p(\cdot, s) n(\cdot, s)$. Eq. (22) shows that $E(t)$ becomes negligible as $t \rightarrow 0$ or $t \rightarrow +\infty$, as expected, meaning that the predicted (computed) stationary current is independent of the use of (19) or the exact expression (17), as numerically verified in Sect. 6.2. However, for a finite value of time t , the discrepancy between the exact convolution term and its approximation may be non-negligible. A reasonable estimate of the error would require a knowledge on the temporal behavior of the photogenerated carrier densities n and p as a function of time. This knowledge not being available, we can still gain some information on the quadrature error by an analogy with the approximation of the recombination/generation term that is usually carried out in the study of currents in a $p-n$ junction in the inorganic case (see [21]). This analogy suggests that the value of $E(t)$ during the photocurrent transient (i.e., for t sufficiently far from 0 but also sufficiently far from stationary conditions) might become significant if the OSC is operating under high injection conditions, or, equivalently, high current level conditions. Again, this latter statement is numerically verified in Sect. 6.2.

Theorem 2 (Existence of a solution in the transient regime). *Let assumptions (H1)–(H4) be satisfied, and the initial data $\mathbf{U} := (n_0, p_0)$, X_0 and the function Ψ be such that $\mathbf{U} \in (H^1(\Omega_T) \cap L^\infty(\Omega_T))^2$, with $\mathbf{U} > \mathbf{0}$, $X_0 \in L^\infty(\Omega)$ with $X_0 \geq 0$, and $\Psi \in H^1(\Omega_T) \cap L^\infty(\Omega_T)$. Then, setting $\mathbf{u} := (n, p)$, system (20)–(21), supplied with the initial/boundary conditions (4a)–(4c), admits a weak solution (φ, \mathbf{u}) such that:*

- (1) $\mathbf{u} > \mathbf{0}$ a.e. in Ω_T ;
- (2) $\mathbf{u}(\mathbf{x}, 0) = \mathbf{U}(\mathbf{x}, 0)$ and $\mathbf{u} - \mathbf{U} \in L^2(0, T; H_0)^2$;
- (3) $\mathbf{u} \in (C(0, T; L^2(\Omega)) \cap L^\infty(\Omega_T))^2$;
- (4) $\frac{\partial \mathbf{u}}{\partial t} \in L^2(0, T; H_0')^2$;
- (5) $\varphi - \Psi \in L^2(0, T; H_0)$ with $\varphi \in L^\infty(\Omega_T)$,

where $H_0 := \{v \in H^1(\Omega) : v|_{\Gamma_D} = 0\}$ and H_0' is its dual.

Moreover, using (16) and the regularity of X_0 , n and p , we have that

$$X, \frac{\partial X}{\partial t} \in C(0, T; L^2(\Omega)) \cap L^\infty(\Omega_T)$$

with $X(\mathbf{x}, t) > 0$ for all $t > 0$ and for a.e. $\mathbf{x} \in \Omega$.

The proof of Theorem 2 consists of verifying that all of the assumptions (Ei)–(Eiv) of [22], p. 296 are satisfied. It is immediate to see that the functions \tilde{R}_η are positive for $p > 0$ and $n > 0$ and satisfy locally Lipschitz conditions, with a Lipschitz constant which is uniform in time and equal to 2γ . As a matter of fact, for any n', p', n'', p'' and for any \mathbf{x} and t , we have

$$\begin{aligned} |\tilde{R}_n(\mathbf{x}, t, n', p') - \tilde{R}_n(\mathbf{x}, t, n'', p'')| &\leq \gamma (\tau(k_{rec} + k_{diss}) + \tau k_{diss}) |p' - p''| \\ &\leq 2\gamma |p' - p''|, \end{aligned}$$

and the same estimate holds for \tilde{R}_p provided to exchange $|p' - p''|$ with $|n' - n''|$. Moreover, (H2) and (H3) ensure that (20)_{2,3} are uniformly elliptic with uniformly

bounded convective velocities. Then, by applying Theorem 2 of [22], we conclude that Theorem 2 (of the present article!) holds.

5. NUMERICAL DISCRETIZATION

In this section, we illustrate the numerical techniques for the simulation of the full model (1)–(4), as the same approach can be used, with slight modifications, to treat the reduced approximate model (20)–(21). In designing the algorithm presented here, our aim is twofold: on the one hand, it seems natural to try to adapt methods that are known to work efficiently and reliably for transient simulation of inorganic semiconductor devices (see, *e.g.*, [23] Chapt. 6, Sect. 4); on the other hand, as the emphasis of the present paper is on accurately estimating photocurrent transient times, it is necessary to apply advanced time-step control techniques [24, 25]. To this end, our chosen approach is based on Rothe’s method (also known as method of horizontal lines) which consists of three main steps: first, the time dependent problem is transformed into a sequence of stationary differential problems by approximating the time derivatives by a suitable difference formula; then, the resulting nonlinear problems are linearized by an appropriate functional iteration scheme; and, finally, the linear differential problems obtained are solved numerically using a Galerkin–Finite Element Method (G–FEM) for the spatial discretization. Sects. 5.1, 5.2 and 5.3 below discuss in more detail each of these steps; it is worth noting that, with minor modifications, the linearization techniques of Sect. 5.2 can also be applied to treat the stationary model (7).

5.1. Time Discretization. To transform the time dependent problem (1)–(4) into a sequence of stationary problems, we replace the partial time derivative with a suitable finite difference approximation, specifically, the Backward Differencing Formulas (BDF) of order $m \leq 5$ (see, *e.g.*, [24], Sect. 10.1.2). To describe the resulting stationary problem, let $0 = t_0 < \dots < t_{K-1} < t_K < T$ be a strictly increasing, not necessarily uniformly spaced, finite sequence of time levels and assume the quantities $u_1 = n$, $u_2 = p$, X and φ to be known functions of \mathbf{x} for every t_k , $k = 0 \dots K - 1$. Then we obtain:

$$(23) \quad \left\{ \begin{array}{ll} -\operatorname{div}(\varepsilon \nabla \varphi_K) + q (n_K - p_K) & = 0 \\ \sum_{k=0}^m \theta_k n_{K-k} - \operatorname{div} \mathbf{J}_n(n_K; \nabla \varphi_K) - U_K & = 0 \\ \sum_{k=0}^m \theta_k p_{K-k} - \operatorname{div} \mathbf{J}_p(p_K; \nabla \varphi_K) - U_K & = 0 \\ \sum_{k=0}^m \theta_k X_{K-k} - W_K & = 0, \end{array} \right.$$

where $f_k = f(\mathbf{x}, t_k)$ for any generic function $f = f(\mathbf{x}, t)$, and

$$\begin{aligned} U_K &:= U(\nabla\varphi_K, n_K, p_K, X_K, t_K) \\ &= G_n(\nabla\varphi_K, n_K, p_K, X_K, t_K) - R_n(\nabla\varphi_K, n_K, p_K, X_K, t_K) n_K \\ &= G_p(\nabla\varphi_K, n_K, p_K, X_K, t_K) - R_p(\nabla\varphi_K, n_K, p_K, X_K, t_K) p_K, \end{aligned}$$

$$\begin{aligned} W_K &:= W(\nabla\varphi_K, n_K, p_K, X_K, t_K) \\ &= g(\nabla\varphi_K, n_K, p_K, X_K, t_K) - r(\nabla\varphi_K, n_K, p_K, X_K, t_K). \end{aligned}$$

System (23), together with the constitutive relations for the fluxes given in (1b) and the set of boundary conditions (4), constitutes a system of nonlinear elliptic differential equations (1a) coupled to an algebraic constraint equation (1c). In our implementation, the selection of the next time level t_K and of the formula's order m , as well as the computation of the corresponding coefficients $\theta_k, k = 0, \dots, m$, is performed adaptively to minimize the time discretization error while minimizing the total number of time steps via the DAE solver software library DASPK [26, 27]. Notice that, if $m = 1$, we have $\theta_0 = -\theta_1 = \frac{1}{t_K - t_{K-1}}$, $\theta_k = 0, k > 1$, and the temporal semi-discretization of system (1)–(4) coincides with the Backward Euler method.

5.2. Linearization. To ease the notation, throughout this section the subscripts denoting the current time level will be dropped. Let $\mathbf{y} := [\varphi, n, p, X]^T$ denote the vector of dependent variables and let $\mathbf{0}$ denote the null vector in \mathbb{R}^4 . Then, the nonlinear system (23) can be written in compact form as

$$(24) \quad \mathbf{F}(\mathbf{y}) = \mathbf{0}, \quad \text{with} \quad \mathbf{F}(\mathbf{y}) = \begin{Bmatrix} f_\varphi(\varphi, n, p) \\ f_n(\varphi, n, p, X) \\ f_p(\varphi, n, p, X) \\ f_X(\varphi, n, p, X) \end{Bmatrix}.$$

The adopted functional iteration technique for the linearization and successive solution of problem (23) is the Newton-Raphson method. One step of this scheme can be written as

$$(25) \quad \begin{bmatrix} \partial_\varphi(f_\varphi) & \partial_n(f_\varphi) & \partial_p(f_\varphi) & 0 \\ \partial_\varphi(f_n) & \partial_n(f_n) & \partial_p(f_n) & \partial_X(f_n) \\ \partial_\varphi(f_p) & \partial_n(f_p) & \partial_p(f_p) & \partial_X(f_p) \\ \partial_\varphi(f_X) & \partial_n(f_X) & \partial_p(f_X) & \partial_X(f_X) \end{bmatrix}_{(\varphi, n, p, X)} \begin{bmatrix} \Delta\varphi \\ \Delta n \\ \Delta p \\ \Delta X \end{bmatrix} = \begin{bmatrix} -f_\varphi(\varphi, n, p) \\ -f_n(\varphi, n, p, X) \\ -f_p(\varphi, n, p, X) \\ -f_X(\varphi, n, p, X) \end{bmatrix}$$

where $\partial_a(f)$ denotes the Frechét derivative of the nonlinear operator f with respect to the function a . More concisely, we can express (25) in matrix form as

$$\mathbf{J}(\mathbf{y}) \Delta\mathbf{y} = -\mathbf{F}(\mathbf{y}),$$

where \mathbf{J} is the Jacobian matrix and $\Delta\mathbf{y} := [\Delta\varphi, \Delta n, \Delta p, \Delta X]^T$ is the unknown increment vector. The exact computation of all the derivatives in the Jacobian on the left hand side in (25) can become quite complicated if the full model for all the coefficients (most notably the electric field dependence of k_{diss} , μ_n and μ_p) is taken into account. Moreover, this would require cumbersome modifications to the solver code whenever a new coefficient model is to be implemented. One alternative could be to employ a staggered solution algorithm, often referred to as Gummel-type approach in the semiconductor simulation context [28, 29]. The decoupled

approach is well known to be more robust as compared to the fully coupled Newton approach (25) with respect to the choice the initial guess and also less memory consuming. As in this particular study we can rely on the knowledge of the system variables at previous time levels to construct a reasonable initial guess and as we are dealing with an intrinsically one-dimensional problem (see Sect. 6), memory occupation is not likely to be a stringent constraint, so that we adopt a quasi-Newton method where, rather than the exact Jacobian $\mathbf{J}(\mathbf{y})$, we use an approximation $\tilde{\mathbf{J}}(\mathbf{y})$ in which the dependence of the mobilities, of the diffusion coefficients and of the dissociation coefficient on the electric field is neglected. This approach has the further advantage of facilitating the use of a standard software library like DASPK for advancing in time.

5.3. Spatial Discretization and Balancing of the Linear System. Once the linearization described in the previous section is applied, the resulting linear system of PDEs is numerically approximated by means of a suitable G-FEM. Precisely, to avoid instabilities and spurious oscillations that may arise when the drift terms become dominant, we employ an exponential fitting finite element discretization [30, 31, 32, 33]. This formulation provides a natural multidimensional extension of the classical Scharfetter-Gummel difference scheme [34, 35] and ensures, when applied to a carrier continuity equation in the DD model, that the computed carrier concentration is strictly positive under the condition that the triangulation of the domain Ω is of Delaunay type. It is important to notice that, when implementing on the computer the above described procedure, the different physical nature of the unknowns of the system and their wide range of variation may lead to badly scaled and therefore ill-conditioned linear algebraic problems, which in turn can negatively affect the accuracy and efficiency of the algorithm. To work around this issue, we introduce two sets of scaling coefficients, denoted $\{\sigma_\varphi, \sigma_n, \sigma_p, \sigma_X\}$ and $\{\bar{\varphi}, \bar{n}, \bar{p}, \bar{X}\}$, and restate problem (24) as

$$(26) \quad \begin{cases} \frac{1}{\sigma_\varphi} f_\varphi(\bar{\varphi}\hat{\varphi}, \bar{n}\hat{n}, \bar{p}\hat{p}) = 0 \\ \frac{1}{\sigma_n} f_n(\bar{\varphi}\hat{\varphi}, \bar{n}\hat{n}, \bar{p}\hat{p}, \bar{X}\hat{X}) = 0 \\ \frac{1}{\sigma_p} f_p(\bar{\varphi}\hat{\varphi}, \bar{n}\hat{n}, \bar{p}\hat{p}, \bar{X}\hat{X}) = 0 \\ \frac{1}{\sigma_X} f_X(\bar{\varphi}\hat{\varphi}, \bar{n}\hat{n}, \bar{p}\hat{p}, \bar{X}\hat{X}) = 0, \end{cases}$$

where $\hat{\varphi} := \varphi/\bar{\varphi}$, $\hat{n} := n/\bar{n}$, $\hat{p} := p/\bar{p}$ and $\hat{X} := X/\bar{X}$. Solving (26) for the scaled dependent variables $[\hat{\varphi}, \hat{n}, \hat{p}, \hat{X}]^T$ corresponds to solving a system equivalent to (25) where the rows of the Jacobian \mathbf{J} and of the residual \mathbf{F} are multiplied by the factors $\{1/\sigma_\varphi, 1/\sigma_n, 1/\sigma_p, 1/\sigma_X\}$ while the columns of \mathbf{J} are multiplied by the factors $\{\bar{\varphi}, \bar{n}, \bar{p}, \bar{X}\}$. Computational experience reveals that a proper choice of the scaling coefficients might have a strong impact on the performance of the algorithm. For example, to obtain the results of Fig. 4 a suitable choice was found to be that of setting $\sigma_\varphi = 1$, $\sigma_n = \sigma_p = 10^3$, $\sigma_X = 10^2$ and $\bar{\varphi} = 1$, $\bar{n} = \bar{p} = 10^{22}$, $\bar{X} = 10^{19}$ while values differing by more than one order of magnitude from such choice were found to hinder the ability of the DAE solver to reach convergence.

6. NUMERICAL RESULTS

This section is devoted to presenting the results of numerical simulations carried out with the algorithms described in Sect. 5. In particular, in Sect. 6.1 we discuss the simulation results for a realistic BHJ device focusing on the impact of the model parameter values on the turn-on transient time in different operation conditions. Sect. 6.2 is devoted to characterizing the region in the model parameter space where the approximate formula (19) and the resulting reduced model (20) are reliable. In both cases the considered device has a thickness $L_{OSC} = 70nm$ and the contact materials are ITO and Al for the transparent and reflecting contact, respectively. As no external voltage is applied to the device, this results in a total voltage drop across the device $\Delta V = 0.5V$. The relative permittivity constant is $\epsilon_r = 4$ and the operating temperature is $300K$. As the thickness of the device is much smaller with respect to the dimensions in the other directions (typically many orders of magnitude larger) and the donor/acceptor blend is considered to be uniform, the simulations presented here are performed in one spatial dimension, so that the computational domain is modeled as the segment $\Omega = [0, L_{OSC}]$ with the cathode at $x = 0$ and the anode at $x = L_{OSC}$. Also, as the device length is quite small compared to the wavelength of visible light, it is reasonable to consider the photon absorption rate G to be constant in Ω at any $t \in [0, T]$.

6.1. Simulation of a realistic device. In this section we present simulation results of the realistic BHJ device whose data are given in [12]. The computations try to reproduce the measurements that are commonly performed in research laboratories to characterize the device material properties and are meant to show the ability of the model to capture the complex dependence of the turn-on transient time on both the mobility coefficients and the exciton dissociation/recombination dynamics, and the predominance of one or the other of such phenomena depending on the operation conditions, *i.e.* on the intensity of the light to which the device is exposed. Throughout this section we use for the coefficients in the boundary conditions (4) the current injection model of [16, 10] corrected as in [12, 17] to increase the carrier surface recombination rate, thus avoiding the occurrence of spurious charge build-up effects near the contacts. The exciton dissociation coefficient k_{diss} is considered to depend on the electric field according to an Onsager-like model given by the nonlinear formula presented in [10] with the initial separation of the geminate pair set to $a = 1.5nm$, while the recombination k_{rec} rate is constant. The bimolecular recombination coefficient γ depends on the carrier mobilities and on the material permittivity ϵ as resulting from Langevin theory [7], therefore, as we consider here the carrier mobilities to be constant, γ is a constant as well. Figure 3 shows the photocurrent evolution in response to an abrupt turn-on of a light source; for each row in the figure the charge carrier mobilities are kept constant while the exciton recombination coefficient is varied whereas for each row in the figure the mobilities are fixed and the recombination coefficients vary. By comparing Figs. 3(a) and 3(c) to Figs. 3(b) and 3(d) one can notice that the strong impact of the recombination rate coefficient k_{rec} on the transient duration in high illumination conditions (dashed lines) completely overshadows the effect of the carrier transport properties, while in low illumination conditions (solid lines) the importance of the effect of k_{rec} is less apparent so that the transient time is more related to the value of the mobilities.

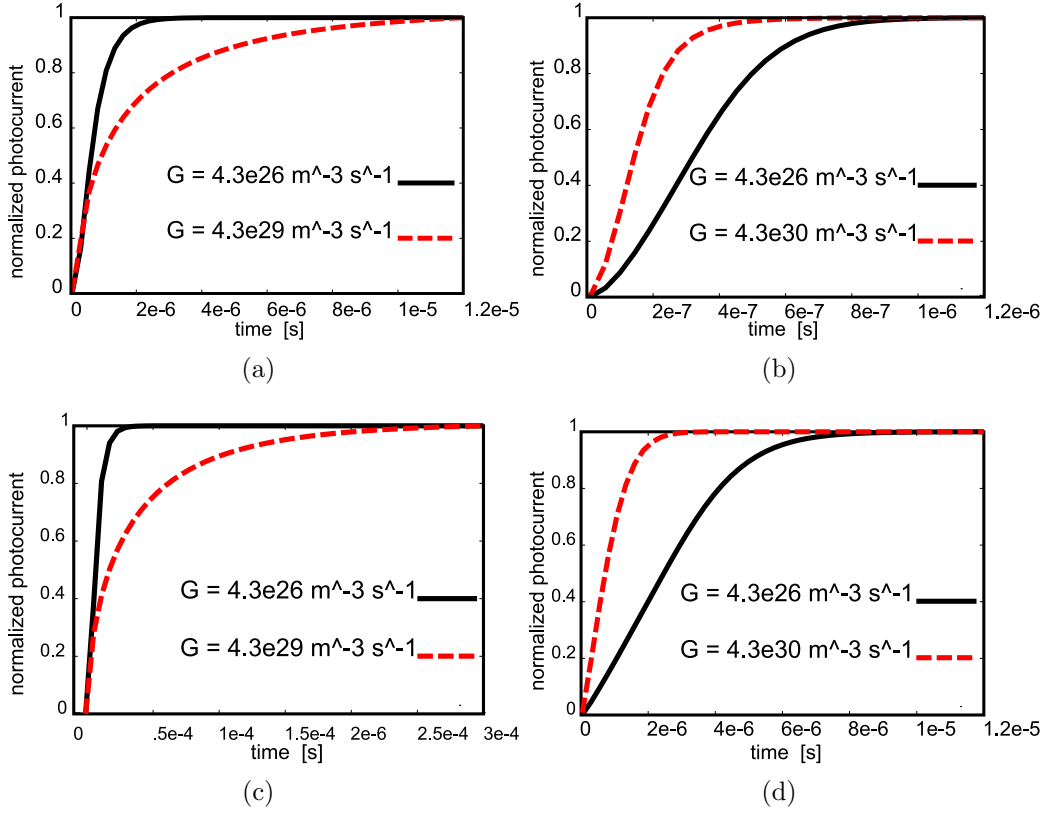


FIGURE 3. Transient currents at low and high intensities with different mobilities and exciton recombination rate coefficients. For (a) and (b) the mobility was $2 \times 10^{-4} \text{ cm}^2 \text{ V}^{-1} \text{ s}^{-1}$ with geminate recombination rate constants $k_{rec} = 1 \times 10^5 \text{ s}^{-1}$ and $1 \times 10^7 \text{ s}^{-1}$ respectively. For (c) and (d) the mobility is $2 \times 10^{-5} \text{ cm}^2 \text{ V}^{-1} \text{ s}^{-1}$ with $k_{rec} = 1 \times 10^4 \text{ s}^{-1}$ and $k_{rec} = 1 \times 10^6 \text{ s}^{-1}$ respectively.

Figure 4 shows the time evolution of the electron density in the device under strong illumination conditions ($G = 4.3 \cdot 10^{30} \text{ m}^{-3} \text{ s}^{-1}$). Hole density is not shown in the figures because, due to the choice of equal mobilities, it is the exact mirror image of the electron density. As previously mentioned, due to the absence of fixed charges (dopants) within the bulk of the device the charge densities do not show the steep interior layers that are the main peculiarity of inorganic semiconductor models and lead to the main difficulties in the numerical simulation of such devices. Also the steepness of the boundary layers is less extreme in the case of organic devices and is further mitigated by the inclusion of finite surface recombination speed in the boundary conditions.

The consistency of the results shown here with those of [12] is a strong indication of the robustness of the numerical algorithm of Sect. 5. Finally, Figure 5 shows the magnitude of the electric field along the device, for low illumination (solid line) the electric field is practically constant throughout the device while for high light intensity (dashed line) its deviation around its mean value $\langle E \rangle = \Delta V / L_{OSC}$ is about 30%.

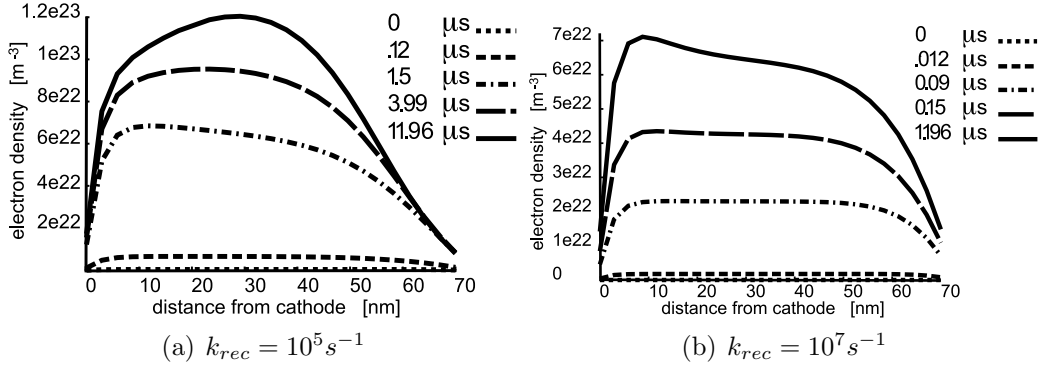


FIGURE 4. Time evolution of the electron distribution at high intensity with (a) high charge generation efficiency and (b) low charge generation efficiency.

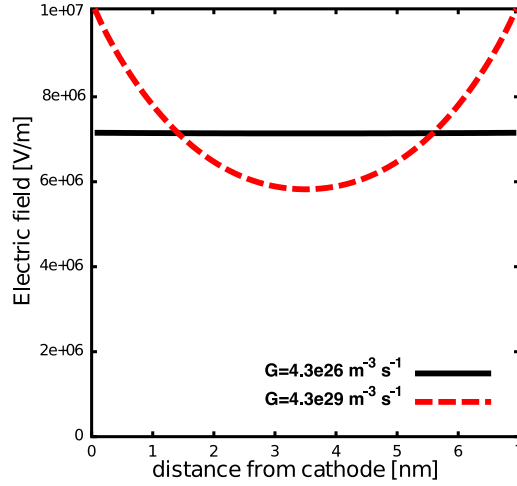


FIGURE 5. Value of the computed electric field for a device with mobilities $\mu_{\eta} = 2 \times 10^{-4} \text{ cm}^2 \text{ V}^{-1} \text{ s}^{-1}$ and recombination rate constants $k_{rec} = 1 \times 10^5 \text{ s}^{-1}$.

6.2. Validation of the simplified model. In this section we wish to estimate the impact of the approximation (19) on the simulation results for parameter values within a physically plausible range. To be consistent with assumptions (H1)-(H4) of Sect. 4, throughout the present section we enforce that all model coefficients be constant by replacing the spatially varying electric field E in the coefficient models by its mean value $\langle E \rangle = -\Delta V / L_{OSC}$. Furthermore we consider carrier recombination at the contacts be instantaneous, so that the boundary conditions (4) degenerate into simple Dirichlet type conditions. The plausibility of these assumptions has been already addressed at the beginning of Sect. 4 and in the discussion of the numerical results of Sect. 6.1. In all subsequent figures, the dashed line refers to the solution computed with the full (3 carrier) model (1)-(4) while the solid line refers to the simplified approximate (2 carrier) model (20)-(21).

Figures 6-7-8 refer to a device under low light intensity conditions and show the impact on the turn-on transient time of the value of the mobilities, of the geminate pair dissociation rate and of the recombination rate, respectively.

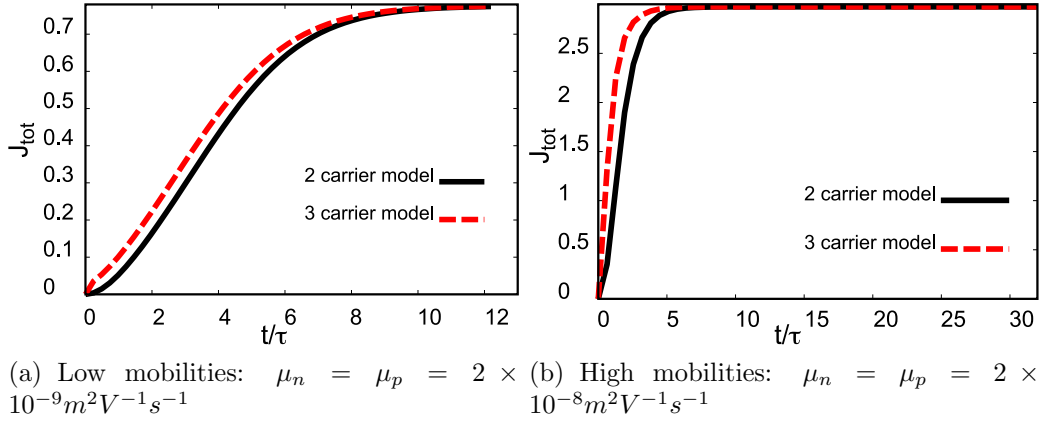


FIGURE 6. Photocurrent transient at low light intensity: effect of mobility on rise time.

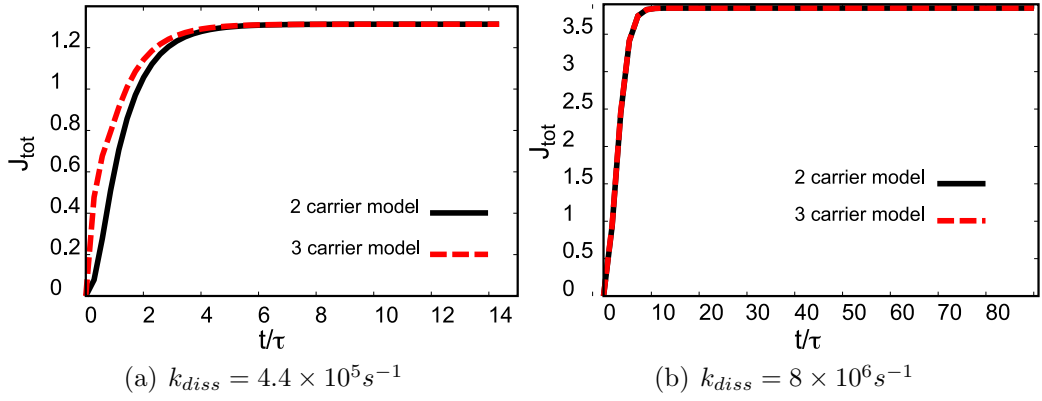


FIGURE 7. Photocurrent transient at low light intensity: effect of dissociation rate on rise time.

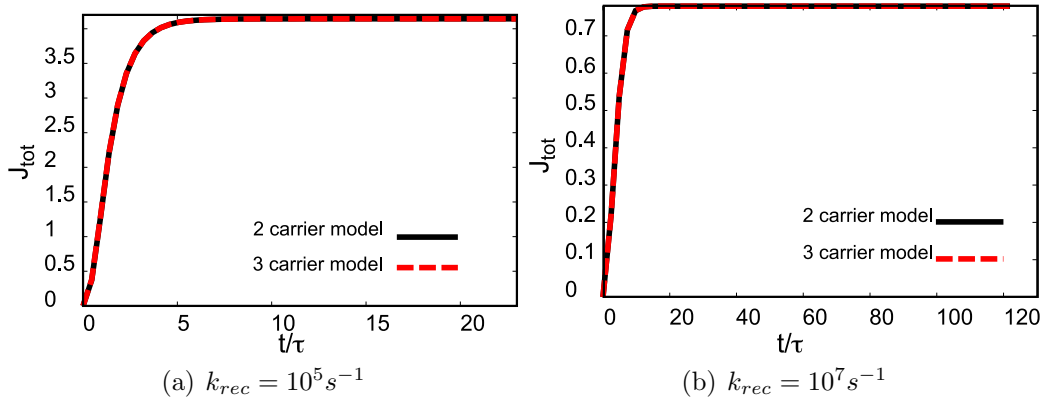


FIGURE 8. Photocurrent transient at low light intensity: effect of geminate pair recombination rate on rise time.

One may observe that, while at low intensity a change of one order of magnitude in the value of the mobility produces an almost equal change in the transient time, at high light intensity (Fig. 9) a similar change in the mobility has an almost negligible

impact. In this latter regime, variations in the dissociation rate k_{diss} (Fig. 10) and, more notably the recombination rate k_{rec} (Fig. 11), produce a more dramatic effect.

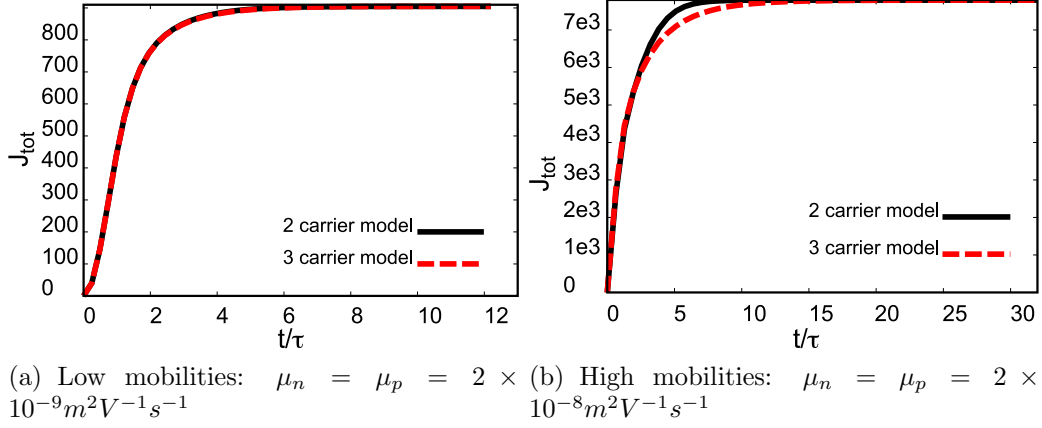


FIGURE 9. Photocurrent transient at high light intensity: effect of mobility on rise time.

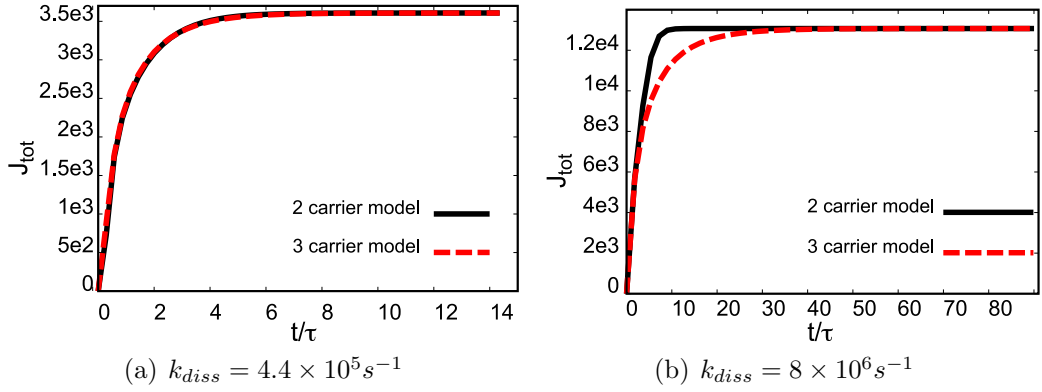


FIGURE 10. Photocurrent transient at high light intensity: effect of dissociation rate on rise time.

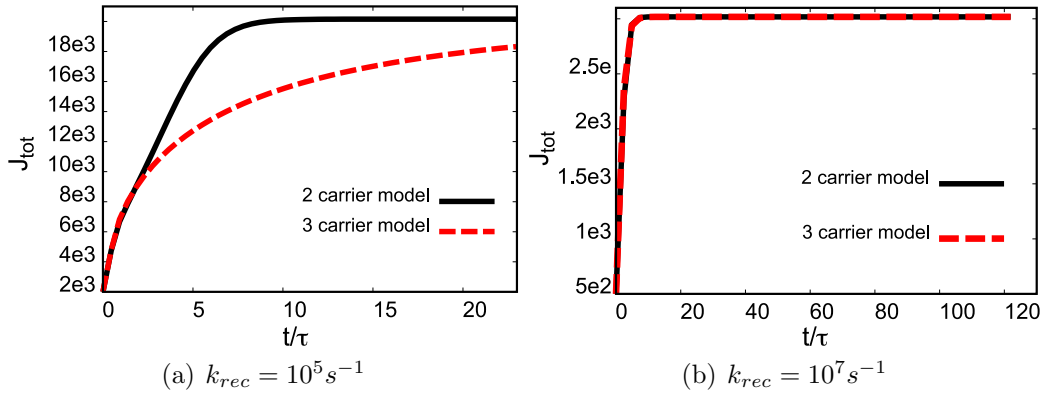


FIGURE 11. Photocurrent transient at high light intensity: effect of geminate pair recombination rate on rise time.

The analysis of the above results displays the complex relation between the transient behaviour of the device and the strongly nonlinear interplay among the several occurring physical phenomena and shows the ability of the simplified model (20)–(21) to capture such behaviour in most circumstances. The only situation where the two models disagree is in the case of a device with high generation efficiency (i.e., a low value of k_{rec}) under high light intensity (cf. Fig. 11(a)). Finally the steady-state current predicted by the reduced model is always in perfect agreement with that of the full model, as expected.

7. CONCLUSIONS AND FUTURE WORK

In this article, we have dealt with the mathematical modeling and numerical simulation of photocurrent transients in nanostructured mono-layer OSCs. The model consists of a system of nonlinear diffusion-reaction PDEs with electrostatic convection, coupled to a kinetic ODE. We have proposed a suitable reformulation of the model which makes it similar to the drift-diffusion system for inorganic semiconductor devices. This has allowed us to prove the existence of a solution for the problem in both stationary and transient conditions and to highlight the role of exciton dynamics in determining the device turn-on time. For the numerical treatment, we carried out a temporal semi-discretization using an implicit adaptive method, and the resulting sequence of differential subproblems was linearized using the Newton-Raphson method with inexact Jacobian. Exponentially fitted finite elements were used for spatial discretization, and a thorough validation of the computational model was carried out by extensively investigating the impact of the model parameters on photocurrent transient times.

Future work is warranted in the following three main areas: 1) extensions to the model; 2) improvement of the analytical results; and 3) development of more specialized numerical algorithms. In detail:

- 1):** we intend to include exciton transport in order to be able to simulate multi-layer or nanostructured devices [11, 8, 36, 37];
- 2):** we aim to extend Theorem 2 to cover the full problem (1)–(4). A possible approach to achieve this result is to apply Theorem 2 locally on a partition of $[0, T]$ into sub-intervals of size Δt , and verify the hypotheses of the Aubin lemma [38] to extract a limiting solution as $\Delta t \rightarrow 0$;
- 3):** starting from the above idea, we intend to devise a numerical algorithm for the local approximation of the full model system over each sub-interval of size Δt using the reduced model (20)–(21). The computer implementation of this approach is straightforward as it basically amounts to a successive application of the formulation discussed in Sect. 5 on each time slab. Furthermore, we intend to improve the robustness of the nonlinear solver with respect to the choice of scaling parameters (cf. Sect. 5.3) by adopting a staggered solution scheme based on some variant of Gummel’s Map [28, 39]. Such scheme could be either employed as an alternative to the current Newton solver or, even more effectively, combined with this latter in a predictor-corrector fashion. The above modifications to the solution algorithm are of great importance in dealing with the simulation of the multidimensional device structures mentioned at item 1).

8. ACKNOWLEDGEMENTS

The very helpful comments by the anonymous referees contributed to improve the quality of the presentation, this contribution was much appreciated and is gratefully acknowledged. The authors wish to thank Prof. Marco Sampietro and Dr. Dario Natali, Dipartimento di Elettronica e Informazione, Politecnico di Milano, Milano (Italy), for many stimulating discussions. They also wish to thank Prof. Joseph W. Jerome for his very careful reading of the manuscript and for his useful comments and suggestions. The first author was partially supported by the European Research Council through the FP7 Ideas Starting Grant program “*GeoPDEs – Innovative compatible discretization techniques for Partial Differential Equations*”. This support is gratefully acknowledged.

REFERENCES

- [1] Climate change 2007: The physical science basis, Tech. rep., IPCC (2007).
- [2] Press release 2785th council meeting environment, Tech. rep., Council of The European Union (2007).
- [3] M. Green, Third Generation Photovoltaics: Advanced Solar Electricity Generation, Springer-Verlag, Berlin Heidelberg, 2003.
- [4] M. Grätzel, Photoelectrochemical cells, *Nature* 414.
- [5] M. Graetzel, Solar energy conversion by dye-sensitized photovoltaic cells, *Inorg. Chem.* 44 (2005) 6841–6851.
- [6] Y. Bai, Y. Cao, J. Zhang, M. Wang, R. Li, P. Wang, S. W. Zakeeruddin, M. Grätzel, High-performance dye-sensitized solar cells based on solvent-free electrolytes produced from eutectic meltcells based on solvent-free electrolytes produced from eutectic melts, *Nature Materials* 7 (2008) 626–630.
- [7] V. Mihailetchi, L. Koster, J. Hummelen, P. Blom, Photocurrent generation in polymer-fullerene bulk heterojunctions, *Physical Review Letters* 93 (21) (2004) 216601 (4pp).
- [8] A. Mayer, S. Scully, B. Hardin, M. Rowell, M. McGehee, Polymer-based solar cells, *Materials Today* 10 (11) (2007) 28–33.
- [9] S. Gunes, H. Neugebauer, N. Sariciftci, Conjugated polymer-based organic solar cells, *Chem. Rev.* 107 (2007) 1324–1338.
- [10] J. Barker, C. Ramsdale, N. Greenham, Modeling the current-voltage characteristics of bilayer polymer photovoltaic devices, *Physical Review B* 67 (2003) 075205 (9pp).
- [11] G. Buxton, N. Clarke, Computer simulation of polymer solar cells, *Modelling Simul. Mater. Sci. Eng.* 15 (2007) 13–26.
- [12] I. Hwang, N. Greenham, Modeling photocurrent transients in organic solar cells, *Nanotechnology* 19 (2008) 424012 (8pp).
- [13] S. L. M. van Mensfoort, R. Coehoorn, Effect of gaussian disorder on the voltage dependence of the current density in sandwich-type devices based on organic semiconductors, *Phys. Rev. B* 78.
- [14] W. Gill, Drift mobilities in amorphous charge-transfer complexes of trinitrofluorenone and poly-n-vinylcarbazole, *J. Appl. Phys.* 55 (12) (1972) 5033.
- [15] G. Horowitz, Organic field-effect transistors, *Advanced Materials* 10 (5) (1998) 365–377.
- [16] J. Campbell Scott, G. Malliaras, Charge injection and recombination at the methal-organic interface, *Chemical Physics Letters* 299 (1999) 115–119.
- [17] I. Hwang, Private communication (2009).
- [18] Atlas user’s manual, Silvaco Co. Support Document (2009).
- [19] P. Markowich, C. Ringhofer, C. Schmeiser, *Semiconductor Equations*, Springer Verlag, Wien, 1990.
- [20] A. Quarteroni, R. Sacco, F. Saleri, *Numerical Mathematics* (2nd Edition), Vol. 37 of Texts in Applied Mathematics, Springer, Berlin Heidelberg New York, 2007.
- [21] S. Sze, K. Ng, *Physics of Semiconductor Devices* (3rd Edition), Wiley, New York, 2006.

- [22] D. Wrzosek, The non-stationary semiconductor model with bounded convective velocity and generation/recombination terms, in: R. B. et al. (Ed.), *Mathematical Modeling and Simulation of Electrical Circuits and Semiconductor Devices*, Vol. 117 of ISNM, Birkhauser Verlag, Basel, 1994, pp. 293–313.
- [23] S. Selberherr, *Analysis and Simulation of Semiconductor Devices*, Springer Verlag, Wien, 1984.
- [24] U. Ascher, L. Petzold, *Computer methods for ordinary differential equations and differential-algebraic equations*, SIAM, 1998.
- [25] E. Hairer, G. Wanner, *Solving Ordinary Differential Equations I*, Springer Series in Computational Mathematics, Springer Verlag, Berlin, 1996.
- [26] P. Brown, A. Hindmarsh, L. Petzold, A description of DASPK: A solver for large-scale differential-algebraic systems, Lawrence Livermore National Report UCRL.
- [27] P. Van Keken, D. Yuen, L. Petzold, DASPK: a new high order and adaptive time-integration technique with applications to mantle convection with strongly temperature- and pressure-dependent rheology, *Geophysical & Astrophysical Fluid Dynamics* 80 (1) (1995) 57–74.
- [28] H. K. Gummel, A Self-Consistent Iterative Scheme for One-Dimensional Steady-State Transistor Calculations, *IEEE Trans. El. Dev.* ED-11 (1964) 455–465.
- [29] C. de Falco, J. W. Jerome, R. Sacco, Quantum corrected drift-diffusion models: Solution fixed point map and finite element approximation, *J. Comp. Phys.* 228 (2009) 1770–1789.
- [30] R. E. Bank, W. M. Coughran, L. C. Cowsar, Analysis of the Finite Volume Scharfetter-Gummel Method for Steady Convection Diffusion Equations., *Computing and Visualization in Science* 1 (3) (1998) 123–136.
- [31] E. Gatti, S. Micheletti, R. Sacco, A New Galerkin Framework for the Drift-Diffusion Equation in Semiconductors, *East West J. Numer. Math.* 6 (2) (1998) 101–135.
- [32] J. Xu, L. Zikatanov, A monotone finite element scheme for convection-diffusion equations, *Math. Comp.* 68(228) (1999) 1429–1446.
- [33] R. Lazarov, L. Zikatanov, An exponential fitting scheme for general convection-diffusion equations on tetrahedral meshes, *Comput. Appl. Math.*, (Obchysljuval’na ta prykladna matematika, Kiev) 1(92) (2005) 60–69.
- [34] D. Scharfetter, H. Gummel, Large signal analysis of a silicon Read diode oscillator., *IEEE Trans. Electron Devices* ED-16 (1969) 64–77.
- [35] F. Brezzi, L. Marini, P. Pietra, Numerical Simulation of Semiconductor Devices, *Comp. Meths. Appl. Mech. Engrg.* 75 (1989) 493–514.
- [36] J. Y. Kim, S. H. Kim, H.-H. Lee, K. Lee, W. Ma, X. Gong, A. J. Heeger, New architecture for high-efficiency polymer photovoltaic cells using solution-based titanium oxide as an optical spacer, *Adv. Mater.* 18 (2006) 572–576.
- [37] D. Xi, C. Shi, Y. Yao, Y. Yang, Q. Pei, Nanostructured polymer solar cells, in: *IRPS 2008, IEEE International Reliability Physics Symposium*, 2008, pp. 178–180.
- [38] J. Jerome, *Analysis of Nonlinear Evolution Systems*, Academic Press, New York, 1983.
- [39] C. de Falco, R. Sacco, J. Jerome, Quantum corrected drift-diffusion models: Solution fixed point map and finite element approximation, *J. Comput. Phys.* 228 (2009) 770–1789.

DIPARTIMENTO DI MATEMATICA “F.BRIOSCHI”, POLITECNICO DI MILANO,, VIA BONARDI 9, 20133 MILANO ITALY